Revue des Composites et des Matériaux Avancés-Journal of Composite and Advanced Materials
Vol. 36, No. 4, August, 2026, pp. 781-797
Journal homepage: http://iieta.org/journals/rcma

Strength vs. Ductility: A Comparative Microstructural Analysis of Stir-Cast Commercially Pure Aluminum Alloy AA1100 Reinforced with Mg and Al_2O_3

Ismail Ibrahim Marhoon[1*], Marwah Ali Harb[2], Ahmed Hashim Kareem[2], Samir Ali Amin[3], Asaad Kadhim Eqal[2], Abdullah Jabar Hussain[4]

[1] Materials Engineering Department, College of Engineering, Mustansiriyah University, Baghdad 10052, Iraq
[2] Mechanical Techniques Department, Amarah Technical Institute, Southern Technical University, Basra 62001, Iraq
[3] Engineering of Refrigeration and Air-conditioning Techniques, College of Engineering Techniques, Al-Farahidi University, Baghdad 10001, Iraq
[4] Department of Computer Techniques Engineering, Al-Mustaqbal University College, Hillah 51001, Iraq

Corresponding Author Email: isibmr@uomustansiriyah.edu.iq

https://doi.org/10.18280/rcma.360408

Received: 2 May 2026
Revised: 10 July 2026
Accepted: 22 July 2026
Available online: 31 August 2026

Keywords:
metal matrix nanocomposites, commercially pure aluminum alloy AA1100, stir casting, tensile testing, Charpy test, Al_2O_3 nanoparticles

ABSTRACT

This paper reports a study of the effects of fixed contents of magnesium (Mg) powder (5 wt.%) and alumina (Al_2O_3) nanoparticles on the microstructure and mechanical properties, aimed at strengthening the commercially pure AA1100 aluminum matrix with nanoparticles of either Mg or Al_2O_3. The systems were fabricated by liquid melt casting at 720–800 °C with mechanical stirring, followed by assessment using advanced microscopy, X-ray diffraction (XRD), tensile testing, and Charpy V-notch impact testing. The added Mg produced a highly reactive mixed solution with a distorted atomic lattice and thermodynamic precipitates of the intermetallic phases Al_3Mg_2 and Mg_2Si. In addition, it promoted the growth of flawlessly bonded nanoscale MgO crystals. This alloy exhibited significant ductility, achieving 60% elongation and consistent strain hardening. It reached an ultimate tensile strength (UTS) of 146.5 ± 3.5 MPa and high dynamic energy absorption of 59 Joules, which is typical of microvoid coalescence. What was produced upon Al_2O_3 addition, on the other hand, was a thermodynamically stable metal-matrix nanocomposite that showed no substantial new intermetallic reaction products. It relied on mechanical interlocking. These stiff nanoparticles imposed strict mechanical requirements arising from Orowan bowing and a dense system of geometrically necessary dislocations (GNDs) due to thermal-expansion mismatch. This composite, therefore, exhibited a very high yield strength of 100 MPa and an UTS higher than 212 ± 6 MPa. Its plastic strain capacity was, however, very limited at 15%, and its very low impact toughness of 12 Joules led to a sudden, very brittle macroscopic fracture due to abrupt, high-severity interfacial decohesion.

1. INTRODUCTION

Commercially pure aluminum alloys, including AA1100, are widely used because of their corrosion resistance, low density, ductility, and ease of processing. Aluminum is also attractive for thermally demanding engineering applications because its high thermal conductivity can provide more efficient heat dissipation than many conventional structural metals [1]. Nevertheless, the relatively low yield strength of commercially pure aluminum limits its use in load-bearing structures. Yet, their structural limitation is a very low yield strength. To broaden the structural use of commercially pure Al, different strengthening mechanisms are to be introduced through engineered methods. Two of the most prominent approaches are the addition of reactive alloying elements (such as magnesium (Mg)) to impart solid-solution strengthening and the addition of ex situ ceramic nanoparticles (such as Al_2O_3) to impart strong strengthening in metal matrix nanocomposites (MMNCs). Both strategies have proven effective in improving the macroscopic yield strength; however, they cause a fundamental change in the matrix's kinematic deformation and often result in an unexpected and severe decrease in ductility and impact properties under dynamic loading. In a study by Mistry et al. [2], Mg additions of 2.5 to 8.5 wt.% were evaluated to determine their effect on grain refinement, which contributes to the mechanical response of pure aluminum. The analysis established that Mg greatly increases hardness and tensile strength by strengthening the solid solution to its maximum level at concentrations up to 4.5%. Further, at this point, it was found that the development of coarse, brittle, intermetallic Al_3Mg_2 at the grain boundaries was affecting the mechanical soundness of the alloy. The study by Haque et al. [3] examined how Mg content and the mechanical corrosion properties of the aluminum alloys depend on the NaCl concentration of the medium (3.5%). Their findings indicated that 5 wt.% Mg is the

best additive for enhancing hardness and flexural strength by refining grains and inhibiting dislocation flow. The study, however, also cautioned that increased Mg concentration hastens localized pitting by undermining the stability of the Al_2O_3 protective surface layer.

Liu et al. [4] have used Cold Metal Transfer-based Wire Arc Additive Manufacturing (WAAM-CMT) to manufacture Al-Mg alloys with superior mechanical properties compared to traditional castings. The authors obtained a very fine, equiaxed grain structure with reduced porosity by maximizing heat input through control of welding parameters. The products exhibited good tensile strength of 382 MPa and improved corrosion resistance due to the favorable presence of the gamma phase ($Al_{12}Mg_{17}$). Saputra and Junipitoyo [5] tested the strengthening effect of aluminum AA1100, with the Mg concentration fixed at 1.2% in the mixture while varying the copper content and heat treatments. The Experiment concluded that the best mechanical integrity, with a tensile strength of 130.8 MPa and an HVN of 90.3, was obtained in the alloy with 4.3% Cu after treatment at 400 °C. Ren et al. [6] investigated the effect of Mg content (5–8 wt.%) in Al-Mg alloys produced via WAAM on their microstructural quality and mechanical performance. In their case, the addition of Mg led to improvements in properties. Still, at concentrations above 6%, surface oxidation becomes excessive, the element burns out severely, and cracks begin to crystallize rapidly. The study set the optimal Mg content at 6%, indicating a good balance between tensile strength (310 MPa) and ductility for additive manufacturing applications. Shah et al. [7] examined the impact of silicon (Si) addition on the microstructural development and mechanical behavior of an Al-4.5Cu-3Mg-0.15Ti casting alloy by evaluating the effects of minor alloying components in high-Mg aluminum systems. Their results show that the addition of Si enables the precipitation of T phases and increases the rate of S-phase formation during aging, resulting in a significant increase in peak yield strength from 270 MPa to 324 MPa in the T6 temper. Lu et al. [8] examined the effects of the cyclical continuous expanded extrusion and drawing (CCEED) technique on the microstructural development and mechanical characteristics of Al-3Mg alloy rods, thereby defining the technique. Their findings indicate that the continuous expansion-extrusion stages play a major role in improving the ductility of materials, i.e., continuous dynamic recrystallization (CDRX). To examine the effects of the solute elements on refinement of the grains, Gubicza et al. [9] compared the microstructural development and mechanical performance of the high-purity aluminum and an Al-3Mg alloy over a broad strain range. Their results indicate that Mg additions pose a serious problem in the recovery process, leading to significantly higher dislocation saturation density and a much smaller grain size of the stable phase, with a stable size of around 0.2–1 mm. Also, as shown in the study, the interaction between Mg solute atoms and dislocations leads to an unusual increase in flow stress with temperature in the early deformation stages. Baridula et al. [10] have examined the process-property relationship in solid-state additive manufacturing via friction stir additive manufacturing (FSAM) of commercially pure AA1100 aluminum alloy, using a Taguchi L4 orthogonal array. They found that the tool tilt angle is the primary determinant of final tensile strength, accounting for 96.78% of the total variance. At the same time, rotational speed plays a leading role in the evolution of Vickers microhardness by influencing frictional heat generation and dynamic recrystallization. Dorta-Almenara and Capace [11] investigated the effect of different Gas Tungsten Arc Welding (GTAW) parameters on microstructural and mechanical stability of the AA6105 aluminum alloys. The researchers found significant recrystallization and precipitate dissolution in the heat-affected zone (HAZ); it was therefore significantly softer and weaker than both the fusion zone and the unaffected base metal. This thermal degradation led to tensile failures that were regularly found only in the HAZ, making it the critical weak point of the weld. In conclusion, the study successfully demonstrated that reducing the welding current effectively restricts excessive grain growth, thereby maximizing the UTS of the joints and yielding the best results.

Zhukov et al. [12] examined the microstructural development and strength of commercial-purity aluminum hardened with Al_2O_3 nanoparticles. In their study, they proved that the addition of nanoparticles, when melt-treated with ultrasonic waves, results in an average grain size reduced to 69–200 min and a uniform distribution of reinforcements. Moreover, the research suggests that Orowan strengthening mismatch and thermal expansion coefficient mismatch are the key factors behind the significant improvements in yield stress, ultimate tensile strength (UTS), and Brinell hardness.

To describe the synergistic reinforcement behavior of hybrid reinforcements in aluminum systems, Na'aim Abd Rahim et al. [13] also evaluated the development and modification of A356 alloy reinforced with Al_2O_3 and multi-walled carbon nanotubes (MWCNTs) via electromagnetic stirring (EMS). Their results indicate that a mixture of 6 wt.% Al_2O_3 and 0.5 wt.% MWCNTs can dramatically transform the grains into a rosette-like form, thereby reducing porosity and maximizing load transfer. To determine the effectiveness of in situ reinforcement methods, Yolshina et al. [14] examined the mechanical and thermal characteristics of aluminum matrix composites reinforced with a morphological crystal of nanoparticles that control the chemical reactivity of the chemical re-inforcer, synthesized via a direct chemical reaction in molten salts. Their study indicates that because these submicron-sized particles are uniformly distributed, it is much easier to increase the matrix's final tensile strength and hardness without compromising thermal stability or the coefficient of thermal expansion (CTE). Furthermore, this molten salt fabrication method offers a cost-effective alternative to conventional powder metallurgy. It also provides strong interfacial bonding, which enables effective load transfer during mechanical deformation. Subhani et al. [15] examined the microstructural and mechanical development of 3 wt.% Al_2O_3 nanocomposites reinforced with Al_2O_3 nanoparticles, prepared via a powder metallurgy route. They investigated the effects of post-processing methods on these systems. They indicate that their initial sintering results in significant increases in hardness and compressive strength of 29% and 144%, respectively, over unreinforced aluminum, but no further improvement in densification with additional thermal and mechanical treatments, such as double sintering or cold pressing. To assess the potential of hybrid reinforcement in lightweight matrices, Mohammed et al. [16] examined the mechanical and thermal properties of aluminum-based nanocomposites with varying contents of Al_2O_3 and graphene oxide (GO). Their results reveal that the combination of these reinforcements, achieved through spark plasma sintering, leads to a drastic increase in microhardness and a considerable decrease in CTE compared to pure aluminum.

These reinforcements have been the subject of extensive

literature individually. Adding magnesium acts as an effective grain refiner, restricting dislocation motion. Consequently, the maximum Mg concentration that maintains a mechanically sound alloy is generally limited to 5 wt.%. On the other hand, mechanical pinning can be very stringent if non-deformable ceramic nanoparticles are added directly, such as Al_2O_3 nanoparticles. Notwithstanding this, an important research gap is the lack of a direct, comparative assessment in the literature that separates the individual contributions of the various microstructural mechanisms underlying reactive alloying effects from those of ex situ ceramic reinforcement, all under the same fixed variables. In addition, ex situ additions of nanoparticles suffer from aggregation and weak mechanical bonding, and the use of reactive particles such as Mg powder can also produce bonded nanoscale ceramics (e.g., MgO), in addition to the more traditional incorporation via solid-solution effects. Such differences between these two mechanisms – in situ and ex situ – remain underexplored in terms of dynamics.

The aim of this study is therefore to directly contrast the evolution of microstructures, kinematic tensile response, and dynamic impact failure mechanisms of the commercial AA1100 aluminum matrix with two basic and opposing strengthening agents. A fixed Mg concentration of 5 wt.% was chosen because it represents the critical maximum for solid-solution efficiency. This concentration was therefore adopted as the reference, with an equivalent quantity of rigid Al_2O_3 nanoparticles introduced for comparison. This paper focuses on the true mechanical compromises between a highly reactive in situ-strengthened system (Mg/MgO) and a stable, mechanically locked nanocomposite (Al_2O_3) with a constant matrix, processing parameters (stir-casting), and weight fractions. This comparative analysis finally offers a clear framework for selecting the optimal reinforcement of a structure based on the required level of compliance and the dynamic impact threshold.

2. THE EXPERIMENTAL MATERIALS

The experimental materials employed in this research are a high-purity aluminum matrix bonded with Mg powder and Al_2O_3 nanoparticles to assess the distinct effects of these additions on microstructural development and mechanical integrity. Aluminum 1100 was selected as the base matrix due to its exceptional corrosion resistance and inherent ductility. However, its unalloyed tensile strength is typically low, measuring approximately 49 MPa. A high-purity aluminum wire (99.8% purity) was used as the matrix material to minimize interference from alloying elements during melting. It is a non-heat-treatable type of wrought alloy that is strengthened either by solid solution hardening or by strain hardening. Commercially pure Mg powder (99.9% purity) was added to the first sample to convert the AA1100 matrix to a binary Al-Mg system, which replicates the properties of the 5xxx series alloys. A 5% Mg additive will cause solid-solution strengthening, as Mg atoms substitute for aluminum in the lattice, creating internal strain that limits dislocation motion. The addition of 5% Mg to the first sample will cause the development of the intermetallic compound. In the case of the second sample, 5 wt.% of Al_2O_3 nanoparticles were added to make an MMNC. Ceramic Reinforcement: α-Al_2O_3 Al_2O_3 nanoparticles were purchased from Sigma-Aldrich (St. Louis, MO, USA), and the average initial particle size was 40 nm, and the purity was 99%. This particular form of Al_2O_3 is a ceramic strengthening material with high compressive strength, high hardness, and thermodynamic stability, which hinder dislocation motion and enable the material to undergo plastic deformation. Energy-Dispersive X-ray Spectroscopy (EDS) was used to determine the elemental composition of the starting materials and the developed samples. Some trace impurities, such as heavy elements like Iron (Fe) and silicon (Si, were present in low amounts. The chemical analysis of the two samples in this investigation is shown in Table 1.

Table 1. The experimental materials' chemical analysis

Element	AA1100 Matrix (%)	Mg Powder (%)	Sample 1 (Al-5% Mg)	Sample 2 (Al-5% Al_2O_3)
Al	99.78	—	Balance	Balance
Mg	0.001	99.9	5.09	Trace
Fe	0.127	—	0.25	Trace
Si	0.056	—	0.154	Trace
Cu	0.006	—	Trace	Trace
Al_2O_3	—	—	—	5.0 (Nominal)

A pure graphite crucible and an electronic temperature controller were installed in an electric resistance furnace to achieve excellent thermal control. The furnace maintains a constant processing temperature of 720 ℃–800 ℃ to support the effective integration of reinforcements. A protective gas was used to prevent unnecessary oxidation and hydrogen absorption, which would otherwise pose risks when melting pure aluminum with reactive Mg. To avoid contamination of the 1100 alloy melt, a ceramic-coated steel stirrer was employed. Stirring was performed continuously at about 750 ℃ to obtain a homogeneous distribution of the reinforcement phases. Sufficient shear energy was provided to uniformly distribute the globular intermetallic particles and nanoparticles throughout the matrix. Kneading must continue until just before pouring into the permanent metallic die (usually mild steel), so that the reinforcement is not deposited due to density differences.

3. EXPERIMENTAL PROCEDURE

Fabrication of the composites was carried out according to a fixed stir-casting procedure to obtain a uniform dispersion of the reinforcement materials and to minimize atmospheric contaminants, including the commercially pure aluminum matrix (AA1100). The process was performed step by step as follows:

1-Matrix Melting: The commercially pure aluminum alloy AA1100 feedstock was placed in a graphite crucible in an electric resistance furnace at a temperature of 800 ℃ for complete melting of the aluminum matrix.

2-Degassing and Fluxing: Protective fluxing for the molten matrix was performed, and common degassing techniques were used to remove impurities and prevent porosity from hydrogen.

3-Prepare for and add reinforcement for the formation of nanoscale MgO by in situ, and for a solid-solution system, 5 wt.% pure Mg powder was added directly to the melt to act as an oxygen scavenger and facilitate solid-solution alloying. Sample 2 (Nanocomposite System): Al_2O_3 (5 wt.%) nanoparticles were dried in an oven for 2 hours at 250 ℃ to

remove surface moisture. In order to avoid initial agglomeration, the preheated particles were introduced dropwise into the vortex generated by the stirrer.

4-Mechanical Stirring: Continuous intensive mechanical stirring was carried out at a temperature of ~750 ℃. This shear energy played a vital role in distributing the non-deformable Al_2O_3 nanoparticles and in the homogeneous precipitation of in situ intermetallics throughout the matrix.

5-The homogenized mixture was immediately poured into a preheated permanent mild steel die. The specific operational parameters governing the stir-casting and in-situ reaction phases were summarized in Table 2 and strictly maintained to ensure complete reproducibility of oxidation control, agglomeration dispersion, and overall casting quality.

Table 2. Comprehensive stir-casting and synthesis parameters

Processing Parameter	Value / Description
Melting Temperature	720–800 ℃
Protective Gas Type	High-purity Argon (Ar)
Gas Flow Rate	3–5 L/min
Impeller Geometry	Ceramic-coated steel stirrer (4-blade pitched turbine)
Stirring Speed	400–450 RPM
Stirring Time	10–15 minutes
Addition Sequence	1) AA1100 melting & fluxing; 2) degassing; 3) reinforcement preheating (at 250 ℃ for 2 hours); 4) gradual vortex addition; and 5) intensive mechanical stirring
Holding Time Before Pouring	0–2 minutes (Stirred until immediately before pouring to prevent settling)
Pouring Temperature	~750 ℃
Die Preheat Temperature	250 ℃

The die was designed to produce cast rods 15 cm high and 2.5 cm in diameter. The samples were left to cool and solidify at room temperature. After being firmly cast, the castings were removed from the mold and were ready for chemical analysis, microstructural characterization, and mechanical testing. A comprehensive set of characterization and mechanical tests is necessary to adequately analyze the microstructural development and the resulting mechanical improvements in AA1100/Mg and AA1100/Al_2O_3 samples. These tests must meet international standards (ASTM), which guarantee academic rigor and reproducibility. The tests for Microstructural Characterization should confirm the placement of the reinforcements and the formation of new phases, including the brittle phase (Al_3Mg_2) in the first sample [17]. The sample was prepared by traditional metallographic methods, which usually include grinding, polishing, and etching with a 0.5% HF solution or Keller's reagent. By doing so, one can observe the grain boundaries, grain size (using ASTM E112), and the transition from coarse to fine to equiaxed grains. Scanning Electron Microscopy (SEM) and EDS provide high-magnification imaging to determine globular intermetallic particles and the distribution of Al_2O_3 nanoparticles. EDS is important for chemical mapping and line analysis to ensure that Mg and Al are present in the matrix and at grain boundaries. X-ray diffraction (XRD) is used to identify phases, i.e., the α-Al matrix and intermetallic phases such as Al_3Mg_2. Mechanical Properties Testing determines the ability of the reinforcements (solid solution vs. ceramic nanoparticles) to withstand deformation and failure. Hardness is determined by applying a specified load with a ball indenter, as per IS 1500 or ASTM E18-22. It is used to assess a material's resistance to localized plastic deformation, which is typically higher when precipitates or secondary particles form. ASTM E8 Tensile Testing Standard specimens are uniaxially loaded to determine the yield strength, UTS, and the percentage elongation. In accordance with ASTM E23, the energy absorbed by the fracture in impact testing (Charpy) is measured to assess the effects of adding Mg or nanoparticles, which typically increase brittleness. In fracture morphology analysis performed after tensile or impact tests, fracture surfaces must be examined using SEM to determine whether the fracture is ductile or brittle. All mechanical tests were repeated for 6 identical specimens (3 per condition) to ensure statistical reliability and reproducibility. Details of the specimen dimensions, notch geometries, and testing parameters are summarized in Table 3.

Table 3. Standardized mechanical testing specifications

Testing Parameter	Specification / Value
Number of Repeats (n)	3 specimens per condition
Tensile Standard	ASTM E8
Tensile Specimen Dimensions	According to the E8 standard dimensions
Tensile Strain Rate	1.0 mm/min
Impact Standard	ASTM E23 (Charpy V-Notch)
Charpy Specimen Dimensions	10 mm × 10 mm × 55 mm
Notch Geometry	2 mm depth, 45° angle, 0.25 mm root radius
Notch Orientation	Transverse-Longitudinal (T-L) orientation relative to casting direction
Data Reporting	Mean ± Standard Deviation

4. RESULTS AND DISCUSSIONS

4.1 Optical microscopy analyses

As-received commercially pure AA1100 aluminum alloy wire is seen in the optical micrograph (OM) in Figure 1(a). One interesting aspect of this image is that it represents the feedstock raw material before melting and stir-casting were performed. Hence, it is included here only as background to the initial constituents for characterization, rather than as a direct structural control in the cast composites themselves. AA1100 is defined as commercially pure aluminum with a minimum content of 99.00%. The rest of that 1.0%, however, is metallurgically essential and is what we are, in fact, looking at in this micrograph: the α-Al solid solution. Due to its commercial purity, the matrix is very ductile and fairly soft. The white/bright specks, which are highly reflective and scattered throughout the matrix, are secondary intermetallic particles in the form of agglomerates [18]. Fe and Si are the main contaminants of AA1100. Since Fe has an almost insoluble nature in solid form at zero degrees (and it is insoluble at almost any degree), it is precipitated during solidification.

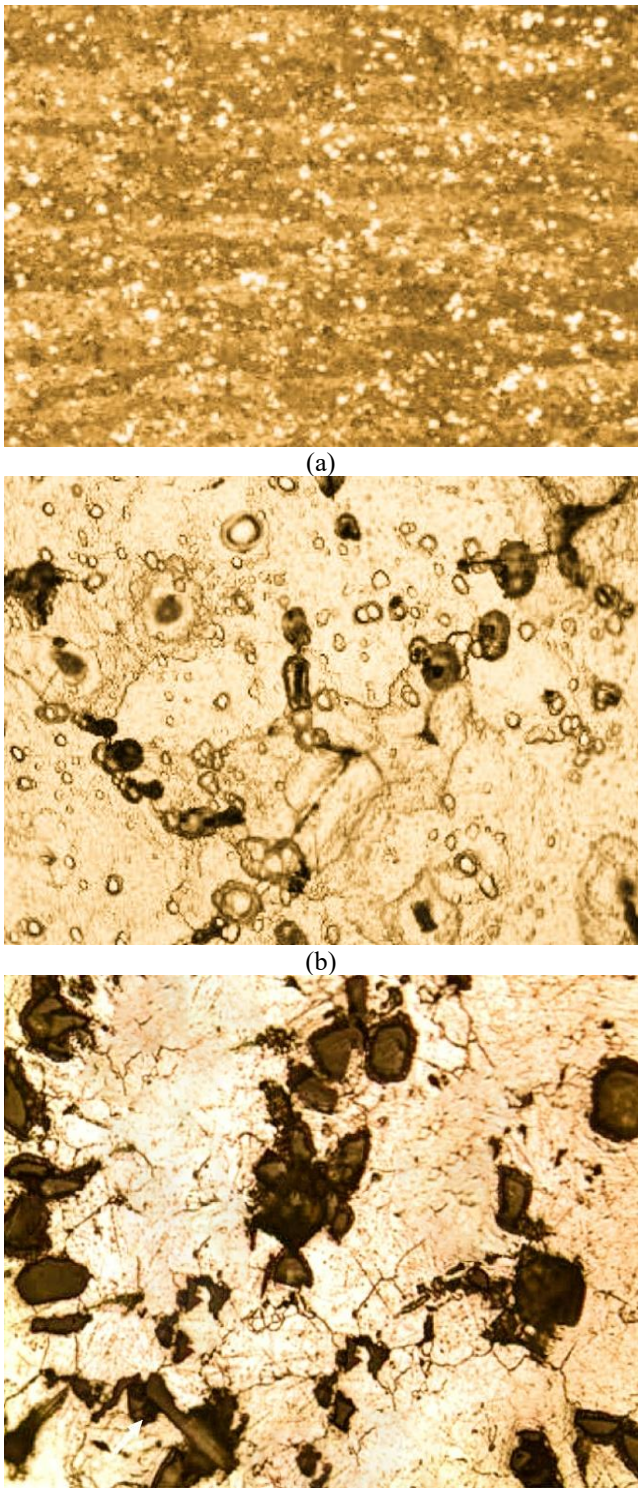

Figure 1. The morphological features of: (a) As-received characterization of AA1100, (b) cast AA1100 with an addition of 5 wt.% of Mg powder, and (c) cast AA1100 with an addition of 5 wt.% of Al_2O_3 nanoparticles, obtained by optical microscopy

These are bright phases that are mainly insoluble Al-Fe and Al-Fe-Si intermetallic (alpha $Al_{12}Fe_3Si$ or Al_3Fe). These harder, more apparent constituent particles commonly polish up in relief and are highly representative of the darker, removed aluminum. Incidence of cold working: the presence of particles is not the only salient feature of this morphology; the spatial distribution and the matrix's general texture are also salient. The received material has evidently undergone extensive plastic deformation, likely by cold rolling. The clearly visible horizontal striations or bands run across the entire field of sight. These are flow lines that reflect a direction of rolling. The initial equiaxed (spherical/polygonal) grains of the cast aluminum are severely crushed and have been extended along the mechanical work performed on them. The horizontal bands are not randomly filled with bright intermetallic particles; the latter follow these bands. The brittle intermetallic particles produced in the initial casting were broken apart and stretched along the rolling direction during rolling. The authors term such arranged groupings of particles "stringers". Although dislocations cannot be observed with an optical microscope (this requires transmission electron microscopy (TEM)), the banding is grossly distorted, indicating a high degree of strain hardening. The driven feedstock wire exhibits a very high degree of deformation due to cold working. Importantly, however, this special strain-hardened microstructure with embedded twisted dislocations completely disappeared once the wire was liquid-melted at 720–800 °C for the liquid matrix of the composites. The actual grain boundaries of the α-Al matrix are not clearly resolved in this micrograph; instead, the etchant attacks regions under high stress and interfaces between constituent particles rather than the grain boundaries themselves [19]. To observe the grain structure of severely deformed aluminum, it is common to perform anodic oxidation (using Barker reagent) and then view it under polarized light.

An intriguing and complex microstructure is shown in Figure 1(b). When 5 wt.% of Mg is introduced to the commercially pure AA1100 base, the thermodynamic environment and physical appearance of the alloy change radically. In contrast to the highly directional, cold-worked matrix of wrought AA1100, the micrograph shows a highly heterogeneous structure with numerous precipitates. The continuous light background represents the α-Al matrix. Mg is highly soluble in aluminum at high temperatures (reaching about 14.9 wt.% at 450 °C). Nonetheless, this does not increase beyond about 2 wt.% at room temperature; below this temperature, the solubility decreases dramatically. The system is supersaturated at room temperature, as the addition is 5% Mg. A substantial amount of that Mg is driven out of solid solution by the cooling rate or subsequent thermal processing (such as sintering or artificial aging), and the hardness and chemical reactivity of the matrix are significantly altered relative to the base (AA1100). Precipitation of the beta-Phase (Al_3Mg_2). The dark, highly concentrated networks and globular structures scattered across the matrix are the most noticeable features in this micrograph. The precipitation of the equilibrium beta-phase, which is usually known as Al_3Mg_2 (or sometimes denoted Mg_5Al_8), is driven by a strong thermodynamic driving force due to the supersaturation of Mg [20]. Nucleation is observed to occur both intergranular (along what would be grain or powder particle boundaries) and intragranular. The clustering indicates microsegregation of Mg in localized regions, which is very common when the alloy is cast at a medium cooling rate or processed by powder metallurgy, where diffusion rates dominate ultimate homogenization. The electronegativity of the beta-phase is very high when compared to the α-Al matrix. This is because the electrochemical difference renders the precipitates highly vulnerable to localized attack. Whilst AA1100 is commercially pure, the subsequent Fe and Si play an essential role when Mg is added. Si is highly affined with Mg. The small bags of Si found in the AA1100 base, too, will react selectively

with the added Mg to create dark and hard intermetallic particles made up of Mg_2Si. Probably, these Mg_2Si constituents are some of the very discrete, darker, localized locations in the micrograph, and they tend to form in advance of the Al_3Mg_2 phase and furnish exceptional pinning locations to control the growth of the grains. Pitting and Preparation Artifacts. The most important thing when reading the particular micrograph is recognizing metallographic artifacts. The dark features appear haloed or as separate craters under a microscope. Because of their brittle nature, the intermetallic phases (Al_3Mg_2 and Mg_2Si) frequently crack and extrude from the softer α-Al matrix during grinding and mechanical polishing, leaving behind microscopic pits. Since the Mg-rich phases are quite anodic, standard etchants (such as Keller or Graff-Sargent) will etch these areas severely. The observed deep, dark globular masses suggest eroded-out pits in which the Mg-rich phases have been dissolved or worn deeper by the etchant, and not the literal physical removal of the precipitate [21].

It is important to recognize that the extreme variation of appearance in Figure 1(b) is partly a metallographic artifact: the deep, dark globular regions in the figure are pits that contain intermetallic inclusions which took up the etchant or were eroded out of the bulk material by it, and the mechanical polishing, and are formed because the intermetallic phase is very anodic and brittle; this intentional precipitation of secondary phases gives the alloy outstanding macroscopic ductility and strength, through providing the highly effective localized pinning sites which inhibit grain growth and govern the continuous solid-solution strain hardening.

Figure 1(c) depicts an informative micrograph of a metal matrix composite (MMC). The use of ceramic nanoparticles in a soft, commercially pure alloy such as AA1100 poses special thermodynamic and kinetic challenges, particularly regarding the Grain Structure and Matrix (α-Al). The main α-Al matrix forms the lighter, continuous background. The grain boundaries of such are not as smudged together as in wrought AA1100, resulting in rather equiaxed polygonal grains. The morphology is strongly indicative of the material having been worked along a path to allow it to form grains without having undergone any rigid subsequent directional deformation-probably a casting process (such as stir casting) or a route in a powder metallurgy (PM) process followed by sintering. The Agglomeration challenge is the most significant point identified in the black, one giant constituent area. 5% Al_2O_3 nanoparticles were added, but they cannot be resolved with an optical microscope (individual particles below 100 nm cannot be resolved). The observed dark regions are on the micron or tens-of-microns scale. As such, the particle agglomeration captured in this micrograph is extreme. Nanoparticles have a very large surface-area-to-volume ratio; hence, their surface energy is very high. Strong Van der Waals forces cause the Al_2O_3 particles to cluster naturally, thereby minimizing this thermodynamic instability. Moreover, Al_2O_3 is highly wetted with molten aluminum. In case such a composite was made by a liquid-state processing route (such as casting), the molten aluminum will tend to reject the ceramic particles rather than coat them, and squeeze them into large, separated agglomerates to reduce the liquid-solid interfacial area. They are not non-selectively scattered in the intragranular areas; rather, they are seriously segregated at the boundaries of the grains as well as on the interdendritic grounds. As solidification proceeds, the solid-liquid interface of growing α-Al grains physically drags the suspension of nanoparticle clusters along behind the freezing front [22]. The clusters are finally caught in the final areas to harden: the grain boundaries. If this were produced through powder metallurgy, this morphology suggests that the Al_2O_3 nanoparticles covered the edges of the much larger AA1100 matrix powders in the mixing stage, while being confined at the edges of the previous particle boundaries in the compaction and sintering stages. Two interacting phenomena occur here at 5%. At 5% addition, there is just enough volume fraction of the reinforcement to agglomerate, so that, at that point, the clusters start joining to form continuous networks along the grain boundaries. The hardness gradient between the very hard Al_2O_3 clusters and the very soft AA1100 matrix is enormous during the preparation of MMCs for optical microscopy. When subjected to grinding and polishing, these brittle agglomerates are highly likely to be ripped off by abrasive forces within the soft matrix, resulting in deep micro-voids and craters. The appearance of the arrowed area, which is rather dark and somewhat shadowy, and the distorted halo around the other large dark areas, is a sure indication that it beholds localized porosity and micro-voids resulting from particle pull-out, rather than merely the planar surface of the ceramic material itself.

4.2 Scanning Electron Microscopy morphology analyses

In Figure 2(a), the SEM micrograph is a high-fidelity image of the microstructure and localized phase distribution in an AA1100 alloy with 5% Mg. The main α-Al matrix forms the broad, dark gray background observed in Figure 2(a) and is relatively smooth. At room temperature, the equilibrium solubility of Mg in Al is extremely low (approximately 1.4 wt.%). The sample has greatly exceeded this solubility limit due to the addition of 5% Mg. This type of strengthening is important for strengthening the solid solution during straining of the aluminum crystal lattice, but the excess Mg must be tipped out of the matrix. These areas are relatively featureless in the matrix itself, as they should be in secondary electron (SE) imaging, unless heavy chemical etching has revealed a specific crystallographic plane. Secondary Phase Precipitation (Bright Regions): The most evident aspect of this micrograph is the highly interconnected, bright network that defines the grain boundaries as well as the interdendritic gallons of the microstructure. These networks are highly consistent with the beta-phase intermetallic, which is Al_3Mg_2 (or sometimes expressed as Al_8Mg_5). Since the 5% Mg addition is supersaturated, the surplus Mg is moved into the high-energy regions of the microstructure, the grain boundaries, as the microstructure cools or sinters [23]. This network can act as a physical hindrance to dislocation movement, significantly increasing the hardness and yield strength of the composite. Nevertheless, since Al_3Mg_2 is highly anodic relative to the α-Al matrix, a continuous grain-boundary network such as this leaves the alloy highly vulnerable to intergranular corrosion and stress corrosion cracking (SCC).

In the matrix shown in Figure 2(b), the striations are straight and parallel. They are not natural microstructural characteristics (such as slip bands); they are metallurgical scratches from polishing. During polishing of a composite containing extremely soft aluminum mixed with much harder Al_2O_3, the matrix becomes smeared, and any Al_2O_3 particles that come off the composite squeeze over the soft α-Al, causing these scratches. The particles have a very slight shadowing effect. As polishing proceeds, the soft Al_2O_3 erosion rate exceeds that of hard Al_2O_3, causing the ceramic

particles to remain slightly above the surface. The Al_2O_3-reinforcement stage is the dark, blocky parts.

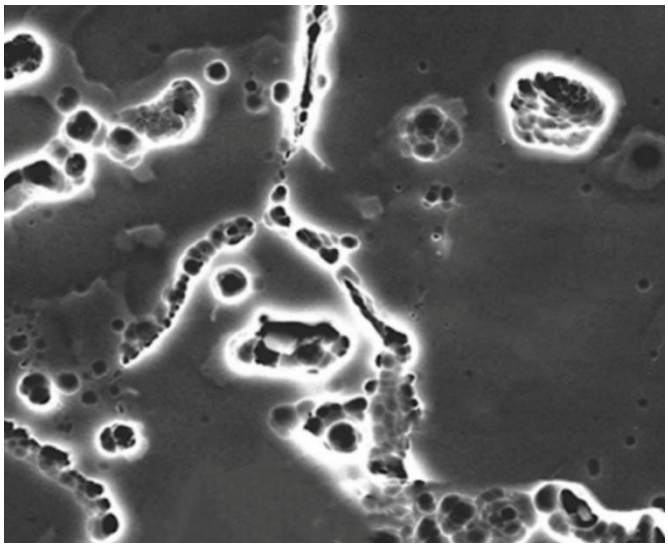

(a)

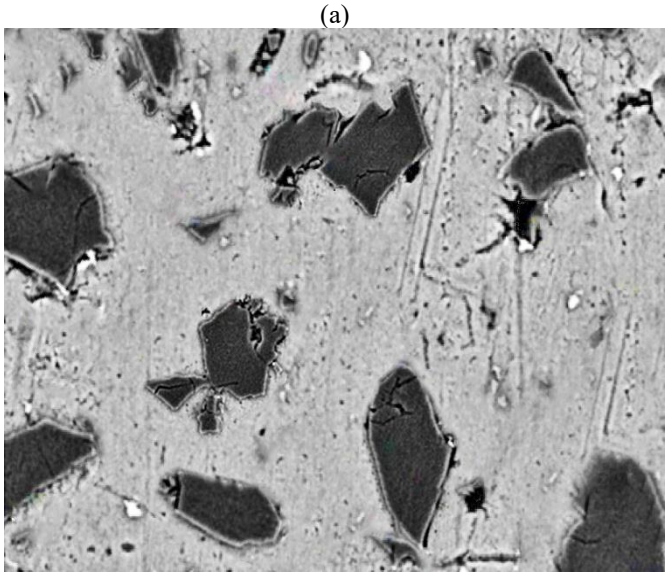

(b)

Figure 2. The Scanning Electron Microscopy (SEM) morphology of AA100 aluminium alloy with additions: (a) with 5% Mg powder addition, and (b) with 5% Al_2O_3 nanoparticle addition

The particles are very jagged, with sharp edges. Sharp edges are considered a serious stress concentrator in an MMC. At such sharp corners in the matrix, under tensile or cyclic loading, cracks will sprout at most. Dark, deep cracks are observed within some of the larger Al_2O_3 particles. Al_2O_3 is extremely brittle. Such internal cracks must have been generated either at the mechanical compaction/mixing stage of synthesis (in the case of powder metallurgy) or by thermal stress on cooling (because of the huge difference in CTE between Al and Al_2O_3 [24]. The interface between nickel oxide particles and the AA1100 matrix governs the mechanical transfer of load. Wettability Issues: dark voids and gaps are visible on the peripheries of some particles. Aluminium and Al_2O_3 are thermodynamically antagonistic in wetting. Molten aluminium (had this been cast) or solid-state aluminium (had this been sintered) does not readily wet the ceramic surface without the addition of wetting agents (such as Mg). Interfacial Porosity vs. Pull-out: The black porosity at the particle edges may represent real interfacial porosity, as these regions are difficult to wet. They may also be of the pull-out type, in which pieces of the delicate Al_2O_3 peel off during grinding and polishing, leaving a hole.

4.3 Transmission Electron Microscopy morphology analyses

A deep examination of the AA1100 + 5% Mg system, using TEM micrographs in Figure 3, indicates a highly dynamic thermochemical environment during processing. Typical evidence of the great affinity of Mg to oxygen is the presence of nanoscale MgO in an Al-5% Mg alloy. Mg participates in the elimination of oxygen as an active oxygen scavenger. Oxygen can never be free during the synthesis of your alloy (through casting metallurgy). It may be dissolved in the melt, entrained by the processing atmosphere, or adsorbed as surface oxygen on raw materials. Since the Gibbs free energy of formation of MgO is rather negative under processing temperatures, the solute Mg will initially react with the available oxygen, forming small volumes of MgO crystals at the nanoscale in the aluminum matrix [25]. This is a formed-in-situ secondary phase that has far-reaching consequences for a material's structural integrity. Figure 3(a) is a general view of the physical interactions between the soft matrix and the freshly developed hard phases in a general manner. The giant, wave-like black sweeps on the left are contours of extinction (extinction contours). Under such a heavily alloyed system as that of Al-5% Mg, the difference in the atomic radius between Al and the large concentration of solute Mg puts heavy strain on the α-Al lattice. Moreover, in situ precipitation forms hard particles, and this (such as those observed in satin MgO clusters around) gives rise to sharp local stress fields. The TEM foil is naturally thin, so it bends into these stress concentrators, bending the crystal planes into diffraction alignment and producing these dramatic, dark bands.

This is evidence of a matrix experiencing significant internal stress directly linked to solid-solution and precipitation hardening. Dark and clumped structures are suspended in the lighter, electron-transparent matrix phases (the MgO and, possibly, the early-stage beta-phase Al_3Mg_2 intermetallic). Note that they are actually clumped into spherical-like accumulations rather than perfectly dispersed. Since they form by the reaction of trace oxygen with Mg, they tend to cluster around microscopic density features (such as grain boundaries) and voids, thereby lowering their surface energy. They are highly effective dislocation blockers because of their size (around 50–100 nm in the case of the clusters).

In Figure 3(b), a high-resolution image, the microstructural advantage of in situ formed precipitates over ex situ additions is evident. The picture shows a clear boundary between the α-Al_2O_3 matrix and an in situ MgO crystal with its (111) lattice planes. Since the MgO is growing internally as a result of the constituent atoms of the alloy itself, the interface is atomically clean. It contains no gaps, absorbed gas layers, or amorphous contamination layers that generally plague artificially mixed lattices. The edges of the aluminum that encounter MgO (111) planes are discontinuous. Such closeness will ensure an ideal metallurgical bond. When the load is applied to this alloy, the stress will flow smoothly from the ductile aluminum to the ultra-hard MgO crystal without the interface rupturing or separating. On a mechanical level, this HRTEM image indicates that the sample has hard, perfectly bonded, nanosized obstacles fully embedded in the matrix. Such dislocations,

finding themselves in motion, will not be able to cut through this MgO crystal but must bend around it (Orowan bowing), imposing enormous demands on the amount of stress applied to them. This mechanism is quite consistent with the observed better strength profiles at the various fixed additions of 5 wt.% Mg [26].

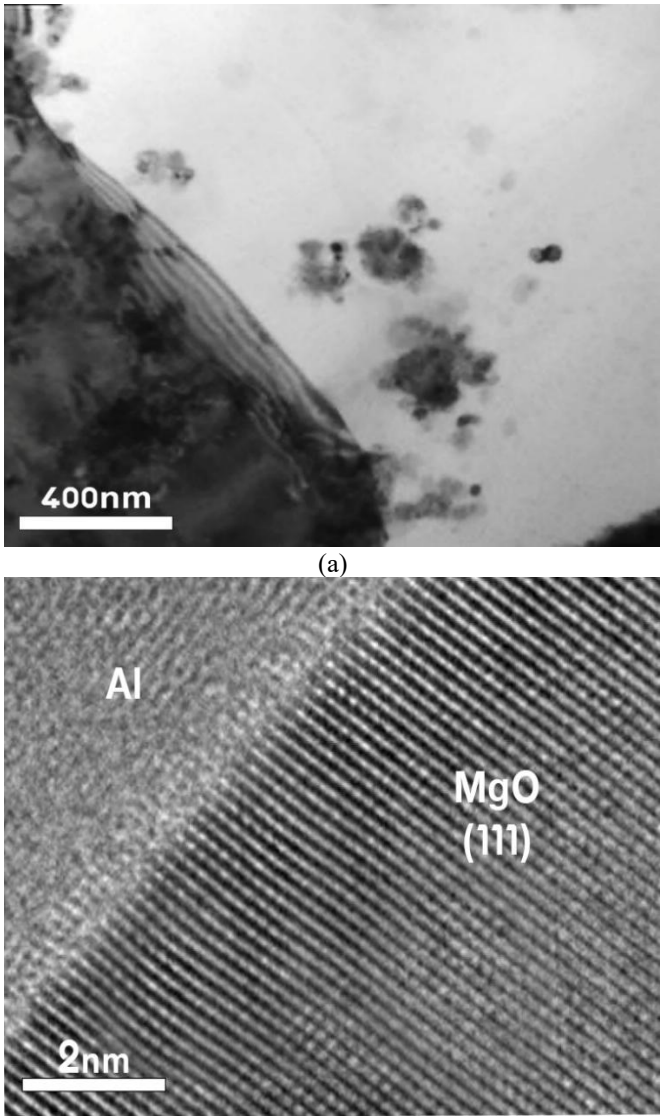

Figure 3. Transmission electron microscopy (TEM) images of AA1100 with 5% Mg addition at (a) 400 nm and (b) 2 nm scale bars

Once a material deforms through its line defects, known as dislocations, they move around. Moving up the crystal lattice of a pure soft metal, such as AA1100, encounters very little resistance from dislocations, which is why pure aluminum is highly malleable. An in-situ formed MgO nanoparticle is an impenetrable barrier. The particles are too hard and have an impeccable metallurgical bond with the matrix, so moving dislocations cannot cut or shear them. They are rather made to prostrate themselves around them. The fact that the dislocation bows changes into a back stress that diminishes considerably more with the applied force required to sustain deformation. The dislocation eventually circumnavigates the particle completely, leaving behind an Orowan ring and proceeding. This extra contribution is most likely the force driving the increase in yield strength. The Orowan-Ashby equation has been modified as the most rigorous calculation of the strength increment (in MPa), which is as follows [27]:

$$\Delta\sigma_{orowan} = \frac{0.13\,Gb}{\lambda} ln\left(\frac{r}{b}\right) \quad (1)$$

where, G is the shear modulus of the aluminum matrix (26,000 MPa). b is the size of the Burgers vector of aluminum (approximately 0.286 nm). r is the mean radius of MgO nanoparticles (which you can measure directly from the TEM images; it is probably in the 2–10 nm range). λ is the interparticle separation, or the effective separation between the particles. The volume fraction (f) of MgO particles in the matrix and their radius (r) have a significant effect on the interparticle spacing. In the case of spherical particles, it is usually approximated as [28]:

$$\lambda \approx r\left(\sqrt{\frac{2\pi}{3f}}\right) \quad (2)$$

Oxygen traces are always present, even in samples melted under controlled conditions. It is present in the air in this neighborhood, either lodged in the microscopic pores of the crucible or in a very thin natural oxide coating on the added 5 wt.% Mg powder. Mg is an immensely stronger thermodynamic contender for oxygen than aluminum. When that 5% Mg powder was stirred into the high-temperature molten AA1100, the atoms of that trace oxygen were immediately "scavenged" by part of the molecules of the molten Mg. So, this process took place within the liquid metal:

$$Mg_2O_2 + O_2 = 2\ MgO$$

As the sample cooled and solidified, the newly formed nanosized MgO molecules crystallized directly from the melt, becoming permanently fixed within the solid aluminum matrix.

In Figure 4(a), TEM is the most dynamic evidence contributing to the reasons why this composite is stronger than the base AA1100 alloy. What is important here is not just the particle and the matrix of peculiar features, but the bright, web-like network in the aluminum. The dark feature marked Al_2O_3 is much larger than 100 nm. On this scale, it is a sub-micron or micron-sized particle, either because the original powder was larger than nominal or because the agglomeration is unfortunately so dense during the mixing/melting stage. The key to this picture is the bright, sharp lines that make a cellular network in the image of the α-Al matrix. These high-density dislocation networks, in particular, create subgrain boundaries. There is a significant difference in the Coefficients of Thermal Expansion (CTE) between aluminum and Al_2O_3. When the composite cooled (or reached room temperature) after melting (or sintering), the aluminum matrix attempted to shrink much faster than the ceramic particles did. This created huge localized interface shear stresses. The aluminum lattice should have become harder to sustain this strain, and in fact, a little swarm of geometrically necessary dislocations (GNDs) was produced. These dislocations knotted and wove themselves into the vivid sub-grain frontiers that you observe here, virtually held in place by the particle of the Al_2O_3. This local work hardening around the ceramic particles correlates with an increase in the material's macroscopic yield strength [29].

The location where the aluminum matrix joins the ceramic addition is indicated by the exact point of contact, as shown in the High-Resolution TEM (HRTEM) image in Figure 4(b). This reveals the nature of (externally added) composite interfaces. The α-Al matrix in the upper right exhibits wonderfully resolved, parallel lattice fringes, indicating high crystallinity. But the diagonal band, marked by the label Al_2O_3, does not exhibit this long-range periodic order; it appears heavily speckled or amorphous. Such a phenomenon in aluminum MMCs is usually due to three causative factors.

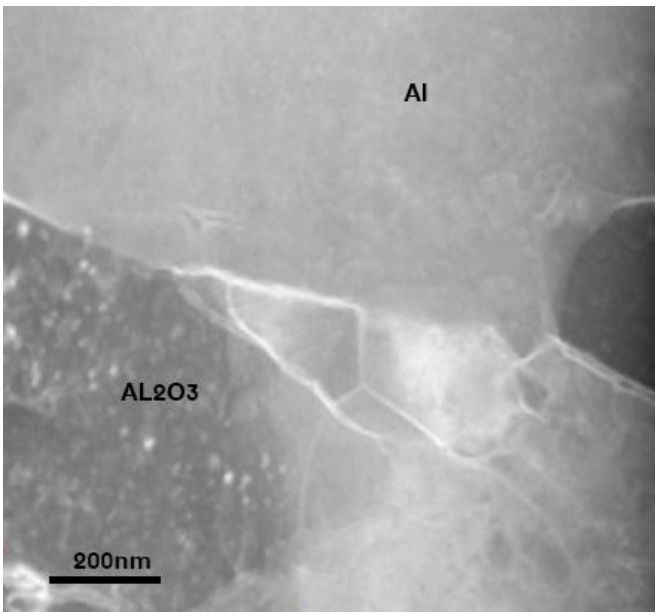

(a)

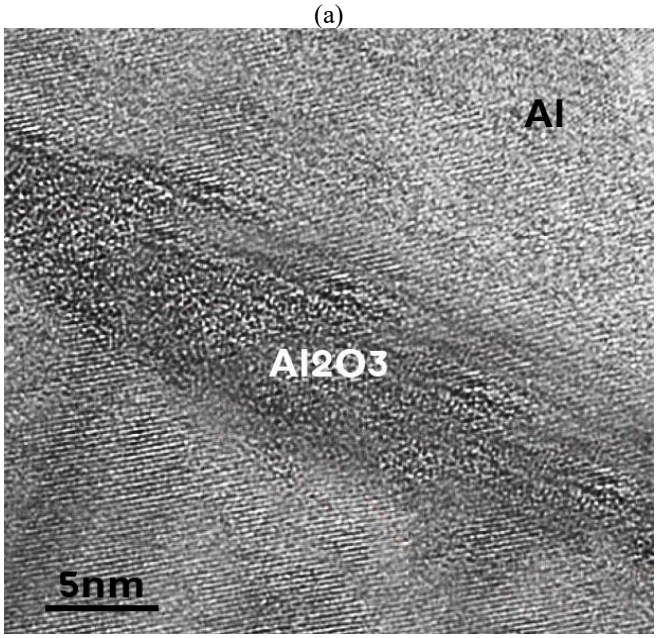

(b)

Figure 4. Transmission electron microscopy (TEM) images of AA1100 with 5% Al_2O_3 addition at (a) 200 nm and (b) 5 nm scale bars

To begin with, nanoparticles typically have a disordered, amorphous outer coating due to their high surface energy. Second, the grains may be an intermediate phase (such as in the possible transitional form of the spinel-like structure, like that of the so-called γ-Al_2O_3) as opposed to the perfectly crystalline corundum (in the form of α-Al_2O_3). Lastly, this can also be an artifact of TEM sample preparation, in which the hard ceramic surface is ruthlessly amorphized by aggressive ion milling, and the interface is physically sharp, with no epitaxy (in which atomic planes of the matrix smoothly slide around the particle). When molten aluminum is unable to wet pure Al_2O_3, the interface is strongly held together by mechanical interlocking, and the compressive residual stresses (due to the CTE mismatch above) lock the matrix around the particle [30]. Here, there is no acute interfacial voiding to observe, as much as possible; however, at the same time, the bond is chiefly physical, not a profound reaction zone of the chemical/metallurgical kind.

During the solidification of the composite (from the manufacturing temperature, say, the solidification temperature of α-Al, 660 °C, to room temperature, 25 °C), the two materials would become unevenly shrunken. The CTE of aluminum (α-Al) is about 23. 6 × 10^{-6} K^{-1}; the CTE of Al_2O_3 (α-Al_2O_3) is 7.2 × 10^{-6} K^{-1}. The Al_2O_3 particle will resist the inflexible Al_2O_3 particle. They can accommodate large volume mismatch by deforming the aluminum lattice, thereby forming a swarm of GNDs in the surrounding aluminum matrix. These distorted dislocations constitute the bright cell networks observed in the TEM micrographs. To obtain the resulting increase in strength, perform this in two operations.

Step A: Determine the enhanced dislocation density. The density of dislocations that are caused by this thermal mismatch is given by the following equation developed by Arsenault and Shi [31]:

$$\Delta\rho = \frac{12f\Delta\alpha\Delta T}{bd(1-f)} \tag{3}$$

where,

• f = volume fraction of the particles (0.05).

• $\Delta\alpha$ = the difference between the CTE of the matrix and particle (16.4 × 10^{-6} K^{-1}).

• ΔT = the temperature drop during cooling (660°C − 25°C = 635 °C).

• b = the Burgers vector of the Al_2O_3 matrix (0.286 × 10^{-9} m). (The original manuscript draft contained a typo here, listing the unit as 10^{-6} K^{-1}. This has been corrected to meters to align with the accurate values you provided later in the text).

• d = the average diameter of the Al_2O_3 particles (in mm).

• 12 = a geometric constant that takes the shape of a particle into account.

Step B: Determine the increment of yield strength(s) ($\Delta\sigma$ CTED). On finding the number of new dislocations generated, using the Taylor relation to determine the amount they prevent plasticity (increasing yield strength) [32]:

$$\Delta\sigma_{CTE} = \beta.G.b.\sqrt{\Delta\rho} \tag{4}$$

where, β is the material constant 1.25 (FCC metals, such as aluminum, usually). G is the aluminum-matrix shear modulus (26,000 MPa). b is the Burgers vector 0.286 × 10^{-9} m.

4.4 Energy-Dispersive X-ray Spectroscopy results analysis

The two reinforced aluminum alloys developed during the current research were also critically characterized using EDS spectra (Figure 5), which served as an in-depth tool for validating the sample synthesis. The base MatrixAA1100 Identification in both spectra shows a predominant aluminum peak at about 1.48 keV, associated with the primary matrix of

the high-purity (99.8) AA1100, which was taken to melt. Both samples show small peaks at Si and Fe at 1.74 and 6.40 keV, respectively. These are inherent constituent intermetallic phases, such as Al3Fe or α-AlFeSi, as is the norm for the 1100 series specification. The AA1100 + 5 wt.% Mg Powder spectrum of Sample 1 in Figure 6(a) is confirmation of the success of converting the matrix to a binary Al-Mg system to replicate the characteristics of 5xxx series alloys. The Mg peak (1.25 keV) corresponds to a 5.09% concentration of Mg in the chemical analysis. The EDS results confirm that Mg atoms have replaced Al atoms in the lattice, causing internal strain that prevents dislocation movement and increases hardness. In addition to the matrix, EDS mapping proved very useful for detecting the beta-phase (Mg_2Al_3) intermetallic. These manifest as dark, bead-like chains along the grain boundaries, characteristic of a sensitized microstructure.

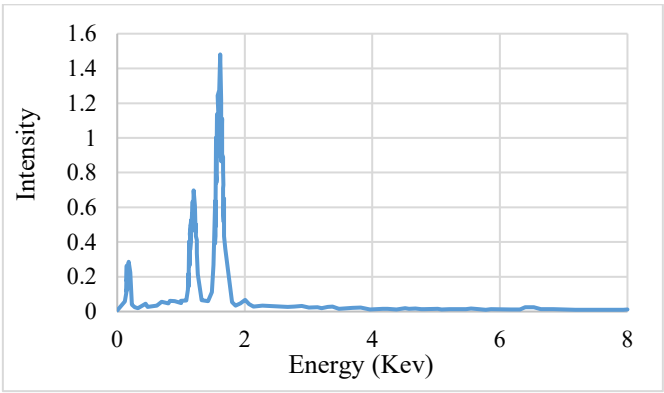

(a)

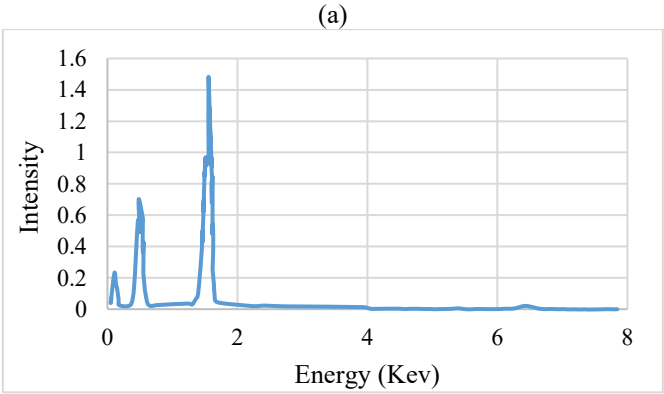

(b)

Figure 5. Energy-Dispersive X-ray Spectroscopy (EDS) results: (a) AA1100 with 5% Mg, and (b) AA1100 with 5% Al_2O_3 nanoparticles

Table 4. Comparative summary of Energy-Dispersive X-ray Spectroscopy (EDS) data

Feature	Sample 1: Al-5% Mg	Sample 2: Al-5% Al_2O_3
Key Reinforcement	Solute Magnesium (Mg) (5.09%)	Ceramic Al_2O_3 (5.0% Nominal)
Strengthening Mechanism	Solid Solution & Intermetallic	Orowan Pinning & CTE Mismatch
Elemental Signature	Mg Peak at 1.25 keV	Oxygen Peak at 0.52 keV
Microstructural Impact	Beaded Mg_2Al_3 at boundaries	Al_2O_3 clusters at boundaries

Sample 2 in Figure 6(b) indicates the material to be an Al_2O_3 reinforced by ceramic particles. Oxygen (O) at a peak (0.52 keV) is the first sign of the reinforcement of the material with Al_2O_3. Compared with Sample 1, this alloy contains trace amounts of Mg. Evidence of ceramic phases: EDS lattice images of this sample showed that a portion of the solidifying material consisted of the ceramic phase, i.e., highly thermodynamically stable, hard nanoparticles of Al_2O_3 that were driven to the edges by growing Al crystals. This caused the particles to become trapped at interdendritic or grain boundaries rather than being perfectly trapped in the lattice [33]. Table 4 compares the EDS data for both samples.

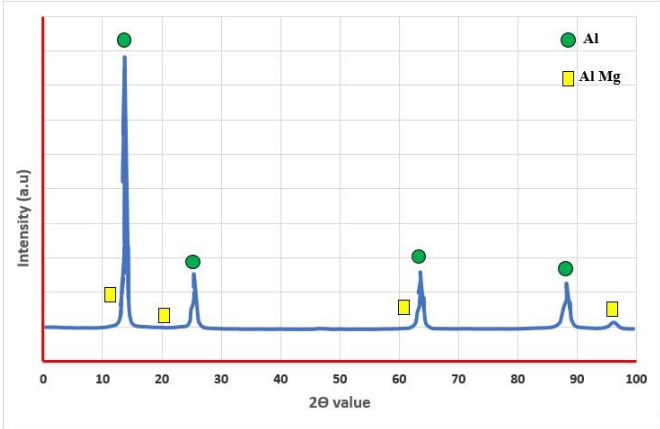

(a)

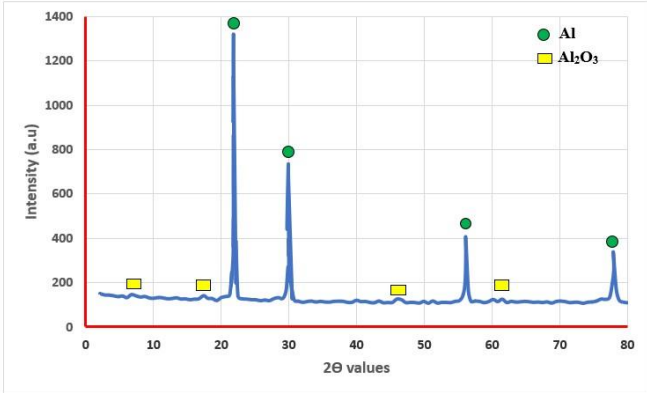

(b)

Figure 6. (a) X-ray diffraction (XRD) pattern of the AA1100 + 5 wt.% Mg powder, (b) XRD pattern of the AA1100 + 5 wt.% Al_2O_3 nanocomposite

4.5 X-ray diffraction analysis

The high-intensity peaks in the XRD plot in Figure 6(a) correspond to the α-Al matrix, which is predominantly face-centered cubic (FCC). Nevertheless, it is no longer pure AA1100; it is a highly alloyed matrix. XRD is used to determine the phases, including the primary α-Al matrix. Due to the very large atomic radius of Mg (1.60 A) compared to the atomic radius of aluminum (1.43 A), the Mg atoms will replace the aluminum atoms in the lattice. The replacement of an atom induces internal, local compressive strain fields within the matrix. The addition of 5% Mg powder can effectively transform the aluminum. The most important data from diffraction, including the standard 2Θ diffraction angles and the assigned (hkl) Miller indices of the primary matrix and all identified secondary phases (Al_3Mg_2, MgO, Mg_2Si, and α-Al_2O_3, Cu-K α radiation), are summarized in Table 5.

This enormous distortion of the lattice is usually observed in an XRD pattern in the form of broadening of the peaks and a slight decrease in the primary α-Al peaks in the final 2 theta

position relative to a pure, unstrained aluminum baseline. This confirms the principle of solid-solution strengthening. Although this causes the primary peaks to shift, the intermetallic beta-phase, formed by the 5% Mg addition, is the crucial phase identified as Al_3Mg_2 (which, in some cases, is referred to as Mg_5Al_8). XRD is specifically used to confirm the presence of elemental transitions between Al and Mg, such as Al_3Mg_2. They are smaller secondary peaks between the primary α-Al peaks, whose positions depend on the volume fraction.

Table 5. 2Θ peaks and assigned (hkl) Miller indices for identified phases

Identified Phase	Crystal Structure	Key 2θ Peaks (Cu-Kα)	Assigned (hkl) Planes
Aluminum (Al)	FCC	38.5°, 44.7°, 65.1°, 78.2°	(111), (200), (220), (311)
Al2O3 (α-Al_2O_3)	Rhombohedral	25.6°, 35.1°, 43.4°, 57.5°	(012), (104), (113), (116)
Al_3Mg_2 (β-phase)	Complex FCC	36.3°, 39.4°, 42.6°	(440), (531), (620)
Magnesium Oxide (MgO)	Cubic	42.9°, 62.3°	(200), (220)
Magnesium Silicide (Mg_2Si)	Cubic	24.2°, 40.1°, 47.4°	(111), (220), (311)

Besides the main Al-Mg phases, there is evidence that highly reactive trace elements remain in their original crystallographic phases, which may manifest as small peaks or background differences in the XRD data. The commercially pure AA1100 base contains small amounts of impurities, namely Si and Fe. Si reacts selectively with Mg to form hard intermetallic particles because of Mg's high affinity for oxygen, and it acts as an active oxygen scavenger during meltdown. The resulting trace oxygen is then reacted with molten Mg to form nanoscale MgO crystals within the aluminum matrix. The resulting nanoscale crystals of the secondary phases extend, imposing far-reaching implications on the material's structural integrity. Figure 6(b) is a textbook sample of an MMNC diffractogram. The most pronounced peaks in the diffractogram in Figure 6(b) are directly linked to the FCC α-Al matrix. Unlike Mg, the ceramic Al_2O_3 nanoparticles do not dissolve into the aluminum crystal lattice, leaving the internal dimensions of the unit cell unchanged. Consequently, the primary α-Al diffraction peaks remain sharp and occur at their unaltered diffraction angles. The smaller, more intense secondary peaks between the dominant aluminum ones are the crystallographic signature of ceramic reinforcement. Al_2O_3 is characterized by high hardness, compressive strength, and thermodynamic stability. Its apparent crystallographic peaks indicate that the nanoparticles were not destroyed or dissolved by such high-temperature processing as 720 °C–800 °C without losing their chemical character or breaking down into the melt. Then, during solidification, the aluminum crystals began to form and physically pushed these forcibly stable particles to the edges, entrapping them at the ends of interdendritic regions or at the borders of the grains, not perfectly within the lattice as they should have been, but at the ends of the interdendritic regions.

Metallurgically, the most important element of this XRD pattern is the relatively explicit lack of unaccounted peaks. Molten aluminum can no longer wet pure Al_2O_3; the interface is forced together by mechanical interlocking. This bond is primarily physical rather than a chemical or metallurgical reaction zone. Since the interface is fixed by a purely mechanical grip rather than by chemical interactions, the XRD pattern reveals a clear absence of new intermetallic reactions, consistent with a brittle character. The trend is neatly divided into two phases: α-Al and Al_2O_3. This two-period XRD pattern would confirm the strengthening mechanisms observed in the sample's tensile test. Since this XRD pattern demonstrates that the Al_2O_3 nanoparticles were not broken in any manner, they are discrete, non-deformable crystals; then any moving dislocations cannot cut through them. The dislocations should instead cut around the nanoparticles through the Orowan bowing mechanism [34]. The large temperature difference in the CTE between the hard ceramic particles and the compliant aluminum matrix leads to a small plastic zone that spreads around each nanoparticle during cooling after fabrication. This forms an excessive concentration of GNDs. It is this combination of harsh Orowan pinning and dense GND networks that causes the tremendous increase in the macroscopic yield stress, up to and including about 100 MPa.

The XRD data indicate that there are two metallurgically quite distinct hardening processes; both the Al-5%Mg solid-solution structure is characterized by a high level of atomic lattice distortion: the integration of the peaks and their broadening, and the uninterrupted formation of the reactive, new intermetallic compound(s) such as Al_3Mg_2. In the 5%-Al_2O_3 nanocomposite, the pattern shows only primary aluminum peaks and clear, consistent ceramic local maxima, with no new chemical reaction products. This crystallographic information ultimately demonstrates that the Mg alloy is strengthened by chemical reactivity and internal lattice strain. In contrast, the Al_2O_3 nanocomposite relies entirely on the physical and mechanical constraints of individual, non-deformable ceramic nanoparticles. Table 6 presents a comprehensive metallurgical comparison of the XRD findings for both synthesized metal-matrix systems.

4.6 Analysis of the tensile test results

The microstructural analyses in the above sections, including those based on optical microscopy, SEM, TEM, and EDS, have identified the underlying crystallographic and phase changes resulting from the addition of Mg powder and Al_2O_3 nanoparticles to the commercially pure AA1100 supporting matrix. At this point, as shown, the characterization shifts from the crystallized, nanoscale level to the macroscopic mechanical response of these engineered systems; tensile testing is used as the critical diagnostic tool to confirm the structure-property relationships theorized in previous sections. The engineering stress-strain curves described below are used to quantitatively assess the effects of the various strengthening mechanisms on the kinematics of material deformation. In particular, this comparison is between solution-solidification hardening by the substitution of Mg with the atomic component, precipitation hardening, and the inflexible mechanical obstructions, Orowan bowing, and thermal dislocation networks induced by the non-deformable ceramic nanoparticles. Results after this point outline the traditional metallurgical trade-offs between improved yield strength and long-term tensile ductility, providing a conclusive assessment of the mechanical soundness of these two specific reinforcement approaches [35]. The distance between the macroscopic strain and yield behaviours of the reactive solid-solution system and the thermodynamically stable

nanocomposite is large, so their respective stress-strain behaviours are plotted on separate axes below so as to maintain readability of the localized yielding behaviours.

Table 6. Comparative X-ray diffraction (XRD) analysis of AA1100-Mg and AA1100-Al_2O_3 composite systems

Metallurgical and Crystallographic Feature	AA1100 + 5 wt.% Mg Powder (Solid-Solution System)	AA1100 + 5 wt.% Al_2O_3 Nanoparticles (MMNC System)
Primary α-Al Matrix Response	The matrix becomes highly alloyed as magnesium (Mg) atoms (1.60 A°) substitute for smaller aluminum atoms (1.43 A°) in the face-centered cubic (FCC) lattice.	The ceramic Al_2O_3 nanoparticles are completely insoluble and do not dissolve into the aluminum crystal lattice.
Lattice Distortion & Peak Shift	The atomic substitution generates severe internal, localized compressive strain fields. This lattice distortion manifests in the XRD pattern as distinct peak broadening and a slight shift of the primary α-Al peaks toward lower 2θ angles.	Because the nanoparticles do not enter the lattice, the internal dimensions of the aluminum unit cell remain completely unchanged. The primary α-Al diffraction peaks remain sharp and occur at their unaltered diffraction angles.
Secondary Phase Identification	Exhibits smaller secondary peaks confirming the precipitation of the equilibrium beta-phase intermetallic, specifically identified as Al_3Mg_2 or Mg_5Al_8.	Exhibits distinct secondary peaks corresponding to crystalline Al_2O_3, confirming the nanoparticles maintained their thermodynamic stability without degrading during the 720 °C–800 °C processing.
Interfacial Chemical Reactions	Highly reactive system. Mg acts as an oxygen scavenger to form nanoscale MgO crystals. Additionally, Mg reacts selectively with trace amounts of silicon (Si) to form hard intermetallic particles.	Explicit lack of unaccounted peaks or new brittle intermetallic reaction products. The interface relies strictly on physical mechanical interlocking rather than chemical or metallurgical bonding.
Overall System Classification	A complex, reactive solid-solution strengthened system characterized by lattice strain and continuous intermetallic phase precipitation.	A clean, highly stable dual-phase system consisting strictly of the α-Al matrix and discrete, non-deformable Al_2O_3 crystals.

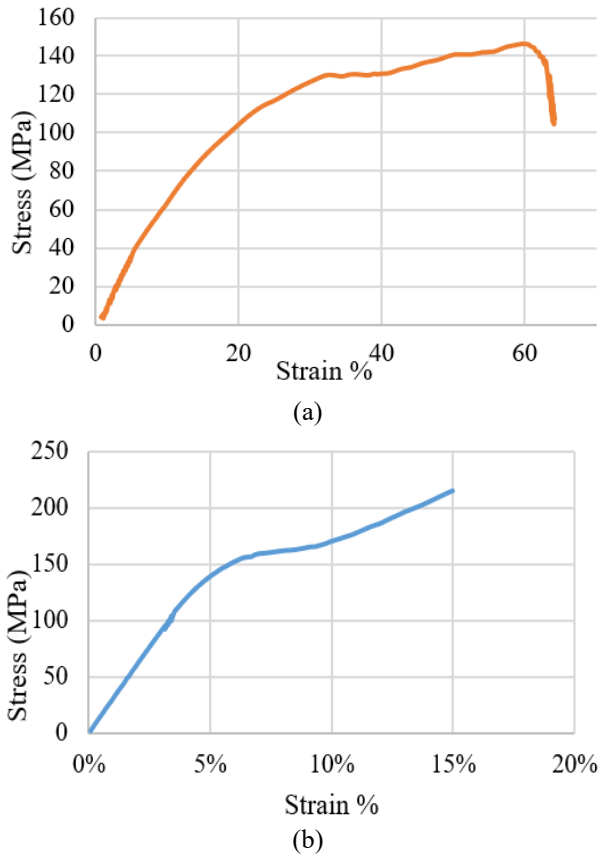

Figure 7. (a) The tensile test results for the AA1100 aluminum alloy with 5% Mg powder addition, and (b) the tensile test results for the AA1100 aluminum alloy with 5% Al_2O_3 nanoparticle addition

Figure 7(a) shows the results of the analysis of the stress-strain curve of the AA1100 matrix with the addition of 5% Mg powder, leading to the appearance of particular and successful micro-integration of the alloying element. A metallurgist views the curve as a recommended example of solid-solution strengthening and extraordinary strain-hardening ability. The curve shows a linear elastic region, followed by a shift in yield stress, after which it becomes macroscopically plastic at 40 ± 2 MPa. Substitutional solute atoms are incorporated in the FCC lattice of aluminum through the introduction of 5% Mg. Since the atomic radius of Mg (~1.60 A°) is much greater than that of aluminum (~1.43 A°), the atomic-scale compressive strain in the matrix is well-localized and spherical in nature [36]. These localized strain fields interact elastically with the stress fields of existing mobile dislocations. The Mg atoms pin the dislocations. A higher applied external stress is required to separate mobile dislocations within these solute atmospheres and to cause the material to exceed its elastic limit, resulting in an increased initial yield point compared with that of the base AA1100. Meanwhile, the most visible part of this curve is the gigantic homogeneous mass of plastic strains. The metal steadily increases in weight up to the yield point, then reaches the final tensile strength (UTS) of 146.5 ± 3.5 MPa, with an engineering strain of 60 ± 2.5%. Dislocation-dislocation interaction is the dominant strengthening mechanism across the vast domain and is essentially altered by the addition of Mg. The pure aluminum matrix has its stacking fault energy reduced by Mg. When the SFE is low, the partial dislocations have a greater distance between them, so the screw dislocations will find it much harder to cross-slip and to circumvent the obstacles. As a result, the dislocations are pushed aside, causing the total dislocation density to soar rapidly in the forest. Dynamic recovery would seem to be the limiting factor, which could have caused the large, constant strain-hardening rate. (σ/ϵ) observed on the curve. This is the very ability to continuously work-harden that enables the material to spread stress evenly and not localize into thinning to such an extent.

The strength of the material peaks near 145 MPa, which is much higher than that of commercially pure AA1100 in the annealed state (typically around 90 MPa). Since the Mg powder additions are complete, this curve is of outstanding

secondary use for assessing the quality of material processing. In the case of poor powder herding, or in the presence of intense oxidation steps on previous particle domains, the material would undergo brittle breakdown during pre-testing or separation across granules, well before it could encounter such tension and strain. The continuous, uniform rise in UTS to a high level suggests very good solid-state alloying, very good inter- and intra-particle metallurgical bonding, and very good load transfer through the matrix [37]. Geometric instability (necking) does not occur until a strain threshold of about 60%. After the acute peak of tensile static deformation, the stress decreases rapidly; according to the considered criterion, macroscopic necking starts at an equivalent point where the material's rate of strain hardening is less than the actual stress ($d\sigma/d\varepsilon \leq \sigma$). Increasing the Mg content to 5% completely prevents this instability, owing to its ability to sustain the high strain-hardening rate. The drop-off in the direct vicinity, immediately after the UTS, is quite steep and hints that when localized void nucleation commences, which it will do at the location of any remaining intermetallic phases, microscopic pores, or the smallest undissolved Mg/oxide particles, void coalescence and ductile rupture take place rather rapidly.

An examination of this stress-strain curve in Figure 7(b) illustrates the deformation kinematics of an MMC in a textbook, incorporating 5 wt.% Al_2O_3 nanoparticles in an AA1100 matrix, essentially transforming the material from a high-ductility, low-strength metal to a high-strength structural composite.

The curve has a sharp initial elastic slope that reaches a yield stress of about 100 ± 4 MPa. It is an enormous improvement over unreinforced AA1100, which typically yields at approximately 30–40 MPa. The rigid Al_2O_3 nanoparticles, as opposed to the Mg addendum (which strengthens upon submersion in the atomic lattice), commonly enhance the matrix due to macro- and microscale mechanical constraints. In elastic deformation, stress is transferred from the object to the soft, compliant aluminum matrix via shear stress across the interface between the matrix and the high-modulus Al_2O_3 nanoparticles. As the fabrication cools, the large CTE mismatch between the ceramic particles and the aluminum matrix causes a localized plastic zone to form around each nanoparticle. This gives a high concentration of GNDs before testing the material. To initiate macroscopic yielding, the applied stress must overcome the resistance of the initial dislocation network.

At the very start of plastic flow, before smooth strain hardening sets in, a characteristic local perturbation, or "juggernaut," appears in the curve. This is one of the most important aspects to consider when writing, because anomalies that cannot be explained are easily flagged by reviewers. In MMCs supported by nanoparticles, this jagged yielding is usually attributed to a local accumulation of micro-stresses that suddenly bursts. Mobile dislocations then interact with the tightly packed ceramic nanoparticles as the matrix begins to flow plastically. It is thought that the serrations indicate the sequential jump of dislocations off pinning sites, or moments of microcracking in micro-sized agglomerates of nanoparticles, which leads to momentary stress reduction in advance of local work hardening of the surrounding matrix, followed by the re-establishment of flow stability.

After the yield aberration, the material undergoes vigorous, continuous strain hardening, steadily increasing to a final tensile strength of 212 ± 6 MPa at an elongation of 15 ± 1.2%. Due to the lack of coherence and shear ability of Al_2O_3 nanoparticles, moving dislocations cannot slice through them. Instead, they need to pass the nanoparticles around via the Orowan bowing mechanism. When dislocations are bowed around the nanoparticles, some of them will be left behind in the form of dislocation loops (Orowan loops). These loops represent new and extremely powerful barriers to later dislocations. This causes a sudden hardening of these forests, which exponentially increases the stress required to bring about further plastic deformation. The high, slanting, stainless-steel-like slope is uninterrupted graphical evidence of a high level of dislocation multiplication and entanglement, such that the matrix ends all primary plastic-strain accommodation at about 15% core strain.

Table 7. Mechanical response and deformation kinematics comparison

Mechanical / Metallurgical Property	AA1100 + 5 wt.% Mg Powder (Solid Solution System)	AA1100 + 5 wt.% Al_2O_3 Nanoparticles (Nanocomposite System)
Macroscopic Yield Strength (σ_y)	40 ± 2 MPa	100 ± 4 MPa
Ultimate Tensile Strength (UTS)	146.5 ± 3.5 MPa	212 ± 6 MPa
Maximum Engineering Strain (Elongation)	60 ± 2.5% (Extensive uniform plastic deformation)	15 ± 1.2% (Reduced plastic strain capacity)
Primary Strengthening Mechanisms	Solid-solution strengthening; atomic lattice distortion via substitutional Mg; Cottrell atmosphere pinning.	Orowan bowing mechanism; load transfer; high density of geometrically necessary dislocations (GNDs) via CTE mismatch.
Yield Behavior	Smooth, continuous transition from elastic to plastic flow.	Yield anomaly/serration at the onset of plastic flow (localized micro-stress release).
Strain Hardening Kinematics	Sustained strain hardening due to lowered Stacking Fault Energy (SFE) and restricted dynamic recovery.	Intense, exponential forest hardening driven by residual Orowan dislocation loops.
Fracture Mechanics & Failure Mode	Delayed geometric instability (necking); eventual ductile rupture via void coalescence at intermetallic phases.	Abrupt macroscopic fracture initiated by interfacial decohesion or rigid particle fracture.

The observed decrease in the matrix's plastic strain potential can be correlated with the addition of 5 wt.% non-deformable ceramic particles. Under severe stresses, the large dislocation pile-ups at the interfaces between the matrix and particles give rise to tremendous local stress concentrations. Since the Al_2O_3 particles will not deform, the strain is relieved either through

interfacial decohesion (the tearing away of the particle) or particle fracture [38]. These serve as nucleation points for the voids. The coalescence of voids occurs very rapidly once initiated, leading to a sudden macroscopic fracture at 15% strain. It is noted that a 15% elongation in a 5% nano-ceramic MMC is a strong outcome, implying high powder dispersion and strong interfacial bonding. A quantitative comparison of the macroscopic mechanical responses in the solid-solution Al-5% Mg alloy and the dispersion-strengthened Al-5%Al_2O_3 nanocomposite is presented in Table 7. It compares the high strain-hardening capability of the Mg addition with the significant enhancement in yield strength achieved by the ceramic nanoparticles.

4.7 Dynamic impact toughness and fractography

To put the static tensile data into perspective with the high-strain-rate application, the dynamic energy absorption of the composite systems was assessed using the Charpy V-notch impact test, as stipulated in ASTM E23. A solid-solution-enhanced system (AA1100 + 5 wt.% Mg) was shown to have outstanding cold energy-absorbing properties, with an average impact toughness of 59 ± 3 Joules. This macroscopic high-energy value strongly supports the observation that, under quasistatic tensile loading, there was extensive uniform plastic deformation (~60% elongation). The fact that the material could be loaded suddenly and violently to 59 Joules implies that the kinetic energy of the pendulum was distributed to fail the material through the rapid multiplication of dislocations and extensive plastic flow, and not through simple premature brittle cleavage at the hot end. To understand the specific micro-mechanisms that preserve this dynamic failure, the post-impact fracture surfaces were examined using SEM. In the fractography of the Al-5% Mg in Figure 8(a), the fracture morphology is classic and highly localized mixed-mode fracture with the overwhelming predominance of microvoid coalescence. Deep, equiaxed dimples that predominate on the fracture surface indicate ductile behavior. These physical residues of highly localized tearing of plastics are fibrous craters. Within the millisecond of contact, the extremely plastic aluminum matrix experienced extreme plastic flow, with the pendulum energy absorbed as the material physically tore while settling under the applied strain. But it is the secondary micro-constituents that determine when this fracture initiates.

The addition of 5 wt.% Al_2O_3 nanoparticles to the AA1100 matrix fundamentally transforms the characteristics of the high-ductility, low-strength metal into a high-strength structural composite, thereby reducing the impact energy.

The essential reduction in the matrix's plastic strain potential is due to increasing the percentage of non-deformable ceramic particles to 5%. Since the material is incapable of large-scale, uniform plastic deformation, it absorbs very little of the pendulum's kinetic energy before disintegration. The visual confirmation of the brittleness of the failure is the graphical depiction in Figure 8(b), which shows very irregular, blocky, and jagged topography dominated by the ceramic secondary phase. These sharp edges are likely to act as significant stress concentrations in an MMC. The material in the Charpy test experiences severe stresses during the violent impact, resulting in large numbers of dislocations at the interfaces between the material and the ceramic particles. It is this dynamic that creates extremely high levels of localized stress within the material.

Within some of the larger dimples are separate, terraced, blocky crystalline structures. These are the brittle intermetallic phases identified during synthesis, namely the equilibrium phases Al_3Mg_2 and Mg_2Si. These stiff intermetallics cannot plastically deform under heavy triaxial stress before the crack tip moves. So, they break through transgranular cleavage planes, becoming the dominant stress-concentration units and sites of imminent inner-hole formation. The discrete localized voids in the nucleated shattered intermetallic were then broken by the ductile matrix (or the α-Al) surrounding the dislocations, which rapidly strained itself to connect the voids and ultimately seal them [39]. The final result, which is 59 Joules of absorbed impact energy, is a direct measure of the mechanical work required to propagate the large-scale microvoid coalescence that establishes a highly ductile failure mode despite the alloy's substantially high yield strength. Adding nanoparticles usually increases the material's brittleness. The absorbed energy is 12 ± 1.5 Joules in the Al_2O_3 sample, indicating that under dynamic, high-strain-rate loading, the macroscopic failure is highly brittle.

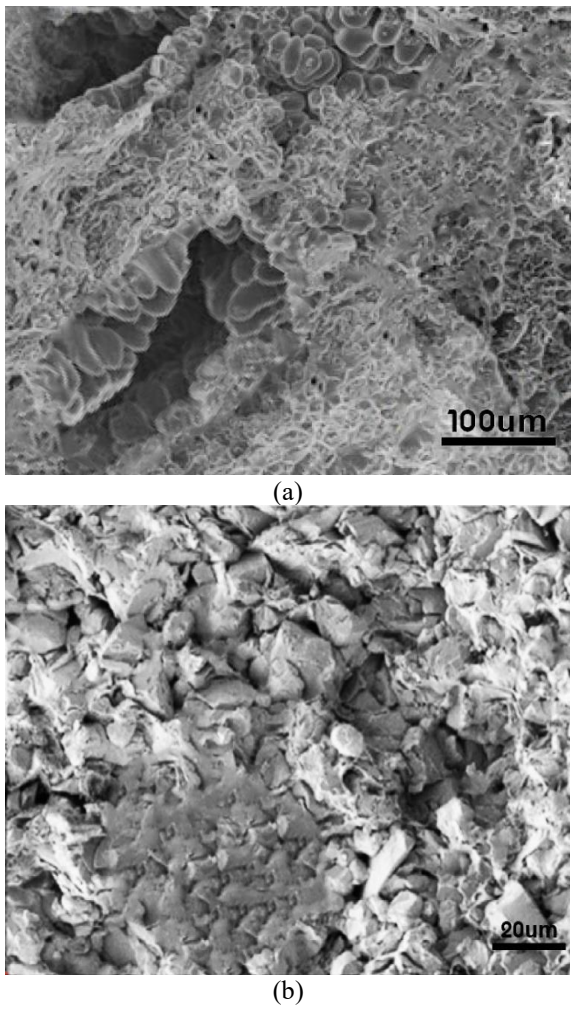

Figure 8. (a) AA1100 with 5% Mg powder, Charpy test sample fracture Scanning Electron Microscopy (SEM) morphology, and (b) AA1100 with 5% Al_2O_3 nanoparticles, Charpy test sample fracture SEM morphology

The SEM image depicts the minute micro-mechanisms of failure resulting from the lack of thermodynamic and mechanical compatibility between the reinforcement and the matrix. Since the highly fragile Al_2O_3 particles would not deform, they would be completely incapable of dissipating the

strain imposed abruptly [39]. Therefore, the stress has to be relieved either by physical separation between the particle and the matrix, known as interfacial decohesion, or by the fracture itself of the ceramic particle. The craters are very irregular, and their sides are very sharp, as seen in the SEM image, providing physical evidence that these particles were crushed or violently ripped from the matrix. Locations of decohesion and fractured particles are instantaneously the nucleation sites for voids in the microstructure. Once voids are initiated at the damaged interfaces, they coalesce very quickly. This rapid interconnection of micro-voids prevents the surrounding aluminum from absorbing energy via progressive tearing, ultimately leading to an abrupt macroscopic fracture. This is broadly consistent with the summarized failure mode of this composite, which indicates a sudden macroscopic failure due to interfacial decohesion or rigid-particle fracture. The impact testing of Charpy demonstrates that the solid-solution Al-5% Mg alloy (59 Joules) possesses a high level of dynamic toughness as compared to the Al-5%Al_2O_3 nanocomposite (highly brittle) (12 Joules). Kinetic energy dissipation occurs efficiently in the Mg-alloyed matrix through extensive plastic flow and ductile microvoid coalescence, even before ultimate failure. Table 8 compares the dynamic impact toughness and fracture morphology results.

Table 8. Comparative analysis of dynamic impact toughness and fracture morphology for Mg and Al_2O_3 reinforced AA1100

Metallurgical Feature	AA1100 + 5 wt.% Mg Powder (Solid-Solution System)	AA1100 + 5 wt.% Al_2O_3 Nanoparticles (Nanocomposite System)
Macroscopic Impact Toughness	Exceptional dynamic energy absorption, recording an average of 59 Joules.	Low dynamic energy absorption, recording an average of 12 Joules.
Macroscopic Failure Mode	Highly ductile failure, supporting the observation of extensive uniform plastic deformation (~60% elongation) under quasi-static loading.	Highly brittle macroscopic failure under dynamic, high-strain-rate loading, resulting in an abrupt macroscopic fracture.
Predominant Fracture Morphology	Classic, highly localized mixed-mode fracture dominated by microvoid coalescence and characterized by deep, equiaxed dimples (fibrous craters).	Very irregular, blocky, and jagged topography dominated by the ceramic secondary phase and characterized by sharp, irregular craters.
Primary Stress Concentrators	Brittle, blocky intermetallic phases (Al_3Mg_2 and Mg_2Si) nestled within larger dimples.	The sharp edges of the rigid, non-deformable Al_2O_3 ceramic particles.
Void Nucleation Mechanisms	Triaxial stress ahead of the crack tip causes transgranular cleavage of the rigid intermetallics, which serve as the immediate nucleation sites.	The ceramic's inability to deform causes extreme localized stress, relieved by either interfacial decohesion (particle pull-out) or rigid-particle fracture.
Energy Absorption Kinematics	The highly malleable α-Al matrix undergoes severe plastic flow, rapidly straining to bridge and seal the nucleated voids. The 59 Joules represents the mechanical work required to drive this extensive void coalescence.	Rapid interconnection of micro-voids prevents the surrounding aluminum matrix from absorbing kinetic energy through progressive tearing. Large dislocation pile-ups at the matrix-particle interfaces lead to unsustainable local stresses.

Comparative evaluations of the tensile and dynamic impact data presented in the previous sections suggest the development of two distinct selection logics for applying these two reinforcement strategies. The in-situ solid-solution system (AA1100 + 5 wt.% Mg) showed outstanding values for dynamic energy absorption (59 ± 3 Joules) as well as high ductility (60 ± 2.5% elongation). This processing route is therefore strongly recommended for applications where impact resistance is desired, and structures are required to withstand loads without failure (e.g., automotive crumple zones or crash barriers, dynamically loaded housings, etc.). In contrast, the nanocomposite system (AA1100 + 5 wt.% Al_2O_3) exhibited exceptional tensile properties (UTS: 212 ± 6 MPa and yield strength: 100 ± 4 MPa) due to the strong Orowan pinning effect. This makes the Al_2O_3 route more appropriate for non-working applications where high stiffness and dimensional stability are prioritized, such as static load-bearing applications that are adequately protected against severe dynamic loading. However, it should be emphasized that the guidelines for material selection recommended herein are valid only within the set of investigated parameters: the reinforcement concentration was set at 5 wt.% only and the operational temperature was room temperature. Further experimental validation of extrapolating these guidelines to other volume fractions or higher temperatures is required.

5. CONCLUSIONS

The different metallurgical/ mechanical strengthening mechanisms of comm. pure AA1100 Al matrix reinforced with both reactive Mg powder and Al_2O_3 nanoparticles were studied. These conclusions are strictly limited to the experimental conditions examined: Synthesis was performed only using the liquid-melt stirring method at a temperature range of 720–800 °C, the reinforcement content was restricted to 5 wt.%, and testing was limited to room temperature. Within these particular parameters, the important points of structural considerations are:

•Phase Evolution and Nanoscale Kinematics: The highly active Mg addition scavenged oxygen to form well-bonded in-situ nanoscale MgO crystals and Al_3Mg_2 precipitates. This combination produced a specific solid-solution and precipitation strengthening effect. Consequently, despite a highly heterogeneous structure, the Mg-alloyed matrix achieved excellent strain hardening and dynamic impact toughness. In contrast, the existing Al_2O_3 nanoparticles, being non-deformable, did not form new compounds with the materials during reactions; they only created dense GND networks under cooling stress due to the larger thermal expansion mismatch.

•At a fixed concentration of 5 wt.%, the solid-solution Mg system exhibited a high elongation of 60 ± 2.5% and a UTS of 146.5 ± 3.5 MPa. The Al_2O_3 nanocomposite demonstrated a vastly superior UTS of 212 ± 6 MPa and a yield strength of 100 ± 4 MPa. However, these strength gains caused a severe reduction in plastic strain capacity. Due to rigid Orowan pinning, macroscopic failure occurred abruptly at an elongation of approximately 15 ± 1.2%.

•Dynamic Impact Toughness: The Mg-alloyed matrix was

found to have an extremely high dynamic energy absorption (59 ± 3 Joules) with ductile microvoid coalescence. The two extremes in material response, rheologic ally compliant and rigid nanoparticles, clearly led to two groups of macroscopic fracture patterns: the localized, quasi-stable damage zone mediated by void coalescence is observed in the case of the compliant (Au) particles and abrupt, brittle fracture is seen for the rigid Al_2O_3 particles, with measured loads for the latter being the lower group with 12 ± 1.5 J.

•Study Limitations: The study only examined mechanical trade-offs up to 5 wt.% reinforcement concentration under the cooling kinetics as in stir casting. However, because intermediate concentrations and temperature variations were not examined, these results cannot be extrapolated as general trends. Future research needs to include a range of weight fractions to fully characterize the operating envelope of these reinforcing mechanisms, as well as high-temperature environmental testing and more sophisticated anisotropic failure criteria.

ACKNOWLEDGEMENT

The authors would like to thank Mustansiriyah University (http://www.uomustansiriyah.edu.iq) in Iraq for supporting the present work.

REFERENCES

[1] Hanan, D.F., Lazuardi, G.M., Trisnoaji, Y., et al. (2024). Thermal and hydrodynamic performance analysis of water-cooled heat sinks using aluminum and structural steel materials. Power Engineering and Engineering Thermophysics, 3(3): 176-188. https://doi.org/10.56578/peet030303

[2] Mistry, V.A., Dave, I.B., Dani, M.S., Rao, V.J. (2025). Influence of magnesium on mechanical properties and microstructure of pure aluminium. Journal of Computer Science, 14(1): 11-21. https://computersciencejournal.org/wp-content/uploads/JCS-1262.pdf.

[3] Haque, M.S., Nomani, M., Akter, A., Ovi, I.A. (2024). Synergistic effect of Mg addition on the enhancement of the mechanical properties and evaluation of corrosion behaviors in 3.5 wt % NaCl of aluminum alloys. Heliyon, 10(3): e25437. https://doi.org/10.1016/j.heliyon.2024.e25437

[4] Liu, Y., Liu, Z., Zhou, G., He, C., Zhang, J. (2022). Microstructures and properties of Al-Mg alloys manufactured by WAAM-CMT. Materials, 15(15): 5460. https://doi.org/10.3390/ma15155460

[5] Saputra, B.W., Junipitoyo, B. (2025). Enhancing the properties of aluminum AA-1100: The effect of Mg and copper additives with heat treatment. SAINSTECH NUSANTARA, 2(1): 12-23. https://doi.org/10.71225/jstn.v2i1.62

[6] Ren, L., Gu, H., Wang, W., et al. (2019). Effect of Mg content on microstructure and properties of Al–Mg alloy produced by the wire arc additive manufacturing method. Materials, 12(24): 4160. https://doi.org/10.3390/ma12244160

[7] Shah, A.W., Ha, S.H., Siddique, J.A., et al. (2023). Microstructure evolution and mechanical properties of Al–Cu–Mg alloys with Si addition. Materials, 16(7): 2783. https://doi.org/10.3390/ma16072783

[8] Lu, R.Q., Zhang, L., Zheng, S.W., et al. (2022). Microstructure, mechanical properties and deformation mechanisms of an Al-Mg alloy processed by the cyclical continuous expanded extrusion and drawing approach. International Journal of Minerals, Metallurgy and Materials, 29(1): 108-118. https://doi.org/10.1007/s12613-021-2342-y

[9] Gubicza, J., Chinh, N.Q., Horita, Z., Langdon, T.G. (2004). Effect of Mg addition on microstructure and mechanical properties of aluminum. Materials Science and Engineering: A, 387-389: 55-59. https://doi.org/10.1016/j.msea.2004.03.076

[10] Baridula, R.R., Jatavallabhula, J.K., Manoj, K.S., Juvvadi, P.K., Kumar, K.R. (2026). Effect of process parameters on strength and hardness of AA1100 fabricated by friction stir additive manufacturing. EPJ Web of Conferences, 345: 01011. https://doi.org/10.1051/epjconf/202634501011

[11] Dorta-Almenara, M., Capace, M.C. (2016). Microstructure and mechanical properties of GTAW welded joints of AA6105 aluminum alloy. Revista Facultad De Ingeniería, 25(43): 7-19. https://doi.org/10.19053/01211129.v25.n43.2016.5293

[12] Zhukov, I.A., Kozulin, A.A., Khrustalyov, A.P., et al. (2019). Pure aluminum structure and mechanical properties modified by Al_2O_3 nanoparticles and ultrasonic treatment. Metals, 9(11): 1199. https://doi.org/10.3390/met9111199

[13] Na'aim Abd Rahim, M., Salleh, M.S., Yahaya, S.H., et al. (2025). Microstructural investigation and mechanical properties of Al_2O_3-MWCNTs reinforced aluminium composite. AIMS Materials Science, 12(2): 318-335. https://doi.org/10.3934/matersci.2025017

[14] Yolshina, L.A., Kvashnichev, A.G., Vichuzhanin, D.I., Smirnova, E.O. (2022). Mechanical and thermal properties of aluminum matrix composites reinforced by in situ Al_2O_3 nanoparticles fabricated via direct chemical reaction in molten salts. Applied Sciences, 12(17): 8907. https://doi.org/10.3390/app12178907

[15] Subhani, T., Alghamdi, A.S., Khaliq, A., Munir, A., Iqbal, M.J. (2023). Investigating the post-sintering thermal and mechanical treatments on the properties of Al2O3 reinforced aluminum nanocomposites. Tehnicki Vjesnik, 30(4): 1003-1009. https://doi.org/10.17559/TV-20221122170946

[16] Mohammed, A.S., Alahmari, T.S., Laoui, T., Hakeem, A.S., Patel, F. (2021). Mechanical and thermal evaluation of aluminum hybrid nanocomposite reinforced with alumina and graphene oxide. Nanomaterials, 11(5): 1225. https://doi.org/10.3390/nano11051225

[17] Hubi, A., Newfal, H., Newal, Z., Dawood, M. (2012). Preparing and studying some mechanical properties of aluminum matrix composite materials reinforced by Al_2O_3 particles. Journal of Babylon University for Engineering Sciences, 20(1): 30-38. https://www.researchgate.net/publication/309512858_Preparing_and_Studying_Some.

[18] Varol, T., Canakci, A., Ozkaya, S., Erdemir, F. (2018). Determining the effect of flake matrix size and Al_2O_3 content on microstructure and mechanical properties of Al_2O_3 nanoparticle reinforced Al matrix composites.

Particulate Science and Technology, 36(3): 312-323. https://doi.org/10.1080/02726351.2016.1248259
[19] Najjar, I.R., Elmahdy, M. (2022). Study of mechanical properties and wear resistance of nanostructured Al 1100/TiO_2 nanocomposite processed by accumulative roll bonding. Journal of Composite Materials, 56(17): 2727-2738. https://doi.org/10.1177/00219983221103636
[20] Yakovtseva, O.A., Mochugovskiy, A.G., Prosviryakov, A.S., Bazlov, A.I., Emelina, N.B., Mikhaylovskaya, A.V. (2024). The microstructure and properties of Al–Mn–Cu–Zr alloy after high-energy ball milling and hot-press sintering. Metals, 14(3): 310. https://doi.org/10.3390/met14030310
[21] Mohammed, M.M.M., Elkady, O.A., Abdelhameed, A.W. (2013). Effect of Al2O3 particles addition on physico-mechanical properties of AL-matrix composites. Open Journal of Metal, 3(4): 72-79. https://doi.org/10.4236/ojmetal.2013.34011
[22] Rocha, F., Simões, S. (2024). Aluminum nanocomposites reinforced with Al_2O_3 nanoparticles: Synthesis, structure, and properties. Journal of Composites Science, 8(1): 33. https://doi.org/10.3390/jcs8010033
[23] Khrustalyov, A., Kakhidze, N., Platov, V., Zhukov, I., Vorozhtsov, A. (2022). Influence of tungsten nanoparticles on microstructure and mechanical properties of an Al-5%Mg alloy produced by casting. Metals, 12(6): 989. https://doi.org/10.3390/met12060989
[24] Dang, X., Zhang, B., Zhang, Z., et al. (2021). Microstructural evolutions and mechanical properties of multilayered 1060Al/Al–Al_2O_3 composites fabricated by cold spraying and accumulative roll bonding. Journal of Materials Research and Technology, 15: 3895-3907. https://doi.org/10.1016/j.jmrt.2021.10.023
[25] Harrell, T.J., Topping, T.D., Wen, H., Hu, T., Schoenung, J.M., Lavernia, E.J. (2014). Microstructure and strengthening mechanisms in an ultrafine grained Al-Mg-Sc alloy produced by powder metallurgy. Metallurgical and Materials Transactions A: Physical Metallurgy and Materials Science, 45(13): 6329-6343. https://doi.org/10.1007/s11661-014-2569-6
[26] Feijoo, I., Cabeza, M., Merino, P., Pena, G., Rey, P. (2019). Age hardening of extruded AA 6005A aluminium alloy powders. Materials, 12(14): 2316. https://doi.org/10.3390/ma12142316
[27] Tian, D., Liu, Y., Yu, J., et al. (2023). A study of silver decoration on carbon nanotubes via ultrasonic chemical synthesis and their reinforced copper matrix composites. Nanomaterials, 13(5): 887. https://doi.org/10.3390/nano13050887
[28] Dieter, G.E. (1986). Mechanical Metallurgy, 3rd ed. New York: McGraw-Hill.
[29] Promakhov, V.V., Khmeleva, M.G., Zhukov, I.A., Platov, V.V., Khrustalyov, A.P., Vorozhtsov, A.B. (2019). Influence of vibration treatment and modification of A356 aluminum alloy on its structure and mechanical properties. Metals, 9(1): 87. https://doi.org/10.3390/met9010087
[30] Gafur, M.A., Ahmed, A.F., Abrar, R., Soshi, S.S. (2023). Development and characterization of aluminium-based metal matrix composites. Materials Sciences and Applications, 14(1): 1-19. https://doi.org/10.4236/msa.2023.141001
[31] Arsenault, R.J., Shi, N. (1986). Dislocation generation due to differences between the coefficients of thermal expansion. Materials Science and Engineering, 81: 175-187. https://doi.org/10.1016/0025-5416(86)90261-2
[32] Casati, R., Vedani, M. (2014). Metal matrix composites reinforced by nano-particles – A review. Metals, 4(1): 65-83. https://doi.org/10.3390/met4010065
[33] Kheder, A.R.I., Marahleh, G.S., Al-Jamea, D.M.K. (2011). Strengthening of aluminum by SiC, Al_2O_3 and MgO. Jordan Journal of Mechanical & Industrial Engineering, 5(6): 533-541.
[34] Mondal, S., Mondal, P., Mishra, D.P. (2023). Research progress on ceramic nanomaterials reinforced aluminum matrix nanocomposites. Materials Science and Technology, 39(15): 1841-1857. https://doi.org/10.1080/02670836.2023.2187153
[35] Ma, Y., Chen, H., Zhang, M.X., et al. (2022). Break through the strength-ductility trade-off dilemma in aluminum matrix composites via precipitation-assisted interface tailoring, 242: 118470. https://doi.org/10.1016/j.actamat.2022.118470
[36] Thirathipviwat, P., Nozawa, S., Furusawa, M., et al. (2023). A correlation between texture evolution and dislocation density in Al-Mg alloys during uniaxial tensile deformation. Materials Letters, 349: 134829. https://doi.org/10.1016/j.matlet.2023.134829
[37] Sarmah, P., Gupta, K. (2024). Recent advancements in fabrication of metal matrix composites: A systematic review. Materials, 17(18): 4635. https://doi.org/10.3390/ma17184635
[38] Gao, X., Zhang, X., Li, A., Geng, L. (2020). Plastic deformation and fracture behaviors in particle-reinforced aluminum composites: A numerical approach using an enhanced finite element model. Journal of Composite Materials, 54(15): 1977-1985. https://doi.org/10.1177/0021998319889110
[39] Zaiemyekeh, Z., Liaghat, G., Khan, M.K. (2021). Effect of Al_2O_3 nanoparticles on the mechanical behaviour of aluminium-based metal matrix composite synthesized via powder metallurgy. Proceedings of the Institution of Mechanical Engineers, Part L: Journal of Materials: Design and Applications, 235(10): 2340-2355. https://doi.org/10.1177/14644207211033626